



A calibration disk for the correction of radial errors from chromatic aberration and rotor stretch in the Optima AUC™ analytical ultracentrifuge

Marielle Stoutjesdyk¹ · Amy Henrickson² · Geoff Minors³ · Borries Demeler^{2,4} 

Received: 3 March 2020 / Revised: 15 April 2020 / Accepted: 28 April 2020 / Published online: 9 May 2020
© European Biophysical Societies' Association 2020

Abstract

Experiments performed in the analytical ultracentrifuge (AUC) measure sedimentation and diffusion coefficients, as well as the partial concentration of colloidal mixtures of molecules in the solution phase. From this information, their abundance, size, molar mass, density and anisotropy can be determined. The accuracy with which these parameters can be determined depends in part on the accuracy of the radial position recordings and the boundary conditions used in the modeling of the AUC data. The AUC instrument can spin samples at speeds up to 60,000 rpm, generating forces approaching 300,000 g. Forces of this magnitude will stretch the titanium rotors used in the instrument, shifting the boundary conditions required to solve the flow equations used in the modeling of the AUC data. A second source of error is caused by the chromatic aberration resulting from imperfections in the UV–visible absorption optics. Both errors are larger than the optical resolution of currently available instrumentation. Here, we report software routines that correct these errors, aided by a new calibration disk which can be used in place of the counterbalance to provide a calibration reference for each experiment to verify proper operation of the AUC instrument. We describe laboratory methods and software routines in UltraScan that incorporate calibrations and corrections for the rotor stretch and chromatic aberration in order to support Good Manufacturing Practices for AUC data analysis.

Keywords Analytical ultracentrifuge · UltraScan · Calibration · Instrumentation · Good manufacturing practices · Reference materials

Electronic supplementary material The online version of this article (<https://doi.org/10.1007/s00249-020-01434-z>) contains supplementary material, which is available to authorized users.

✉ Borries Demeler
demeler@gmail.com

¹ Department of Physics and Astronomy, The University of Lethbridge, 4401 University Drive, Lethbridge, AB T1K 3M4, Canada

² Department of Chemistry and Biochemistry, The University of Lethbridge, 4401 University Drive, Lethbridge, AB T1K 3M4, Canada

³ Technical Services, The University of Lethbridge, 4401 University Drive, Lethbridge, AB T1K 3M4, Canada

⁴ Department of Chemistry and Biochemistry, The University of Montana, 32 Campus Drive, Missoula, MT 59812, USA

Introduction

Analytical ultracentrifugation (AUC) is a first-principle, biophysical method for determining the hydrodynamic parameters of macromolecules in a solution environment (Svedberg and Pedersen 1940). AUC plays an important role in biochemistry and biophysics as a gold-standard characterization method to measure composition (Carruthers et al. 2000) and interactions (Demeler et al. 2010) of biopolymers (Patel et al. (2016)). With the advent of fast computers, sedimentation velocity experiments have become the preferred method to perform AUC experiments (Demeler 2010; Brookes and Demeler 2008). Sedimentation velocity experiments monitor the concentration changes over time occurring in a sector-shaped compartment when the solution is subjected to a centrifugal force field. AUC instruments are able to record the evolving concentration profile as solutes redistribute inside the AUC sample cell, primarily using three types of optical systems: (1) UV–visible absorbance, (2) Rayleigh

interference (measuring refractive index changes), and (3) fluorescence detection (measuring the fluorescence emission of a fluorophore or fluorescent label). Experimental data are collected over time as a sequence of radial scans. The latest AUC instrument commercially available, the Beckman-Coulter Optima AUC™ instrument, features a sensitive UV–visible detection optical system that can rapidly (in as little as 16 s/scan) collect absorbance data between 190–800 nm with a radial resolution of 10 μm . Notably, the instrument allows changes in the detection wavelength during the experiment, enabling the acquisition of multi-wavelength experiments (Gorbet et al. 2015; Hu et al. 2019; Johnson et al. 2018; Demeler 2019; Plascencia-Villa et al. 2016; Zhang et al. 2017). Sedimentation velocity experiments can be simulated by finite element solutions (Cao and Demeler 2005, 2008) of the Lamm equation (Lamm 1929). Fitting of experimental data using these finite element solutions is accomplished by several algorithms (Brookes and Demeler 2006, 2007, 2008; Brookes et al. 2010), which can extract each solute's sedimentation and diffusion coefficient with high resolution, as well as its partial concentration. Importantly, finite element solutions of the Lamm equation require accurate knowledge of the boundary conditions, which include the radial positions of the meniscus and bottom location of the sample cell. Any error in these boundary conditions, or the absolute radial positions collected will affect the fitted values of the sedimentation and diffusion coefficients. This error propagates to the calculations of biomolecular attributes such as anisotropy and molar mass of the solute. The accuracy of sedimentation velocity experiments has long been of particular interest to regulatory agencies and the biopharma industry, which wishes to use AUC for validation of soluble therapeutics (Liu and Shire 1999). A recent multi-laboratory study has highlighted the need for accurate reference materials to provide improved validation for AUC experiments, and to complement the resolution gains afforded by modern analysis software (Zhao et al. 2015).

While investigating the accuracy of the radial recordings made in the current Optima AUC instrument, we noticed the presence of a wavelength dependence on the radial positions collected by the instrument as a result of chromatic aberration, a phenomenon related to the variability of refraction at different wavelengths. This is most likely a result of the angle of the incident light, as it may not be perfectly perpendicular to the plane of observation. A second source of error is apparent when the Lamm equation is solved with incorrect boundary conditions. Typically, the meniscus position is fitted to obtain an optimal position, but the bottom of the cell position is routinely held constant at the known position at rest. However, due to the extreme forces generated during high speed runs, the absolute radial position of the sample cell will shift during the experiment because the

titanium rotor stretches a finite amount, changing the boundary conditions of the experiment compared to either at rest or a different speed. If the experimental data are fitted with the incorrect boundary condition at the bottom of the cell, mismatches are observed in a region where back-diffusion from the bottom of the cell affects the resulting concentration distributions. This back-diffusion effect is most notable for smaller molecules or for experiments performed at low rotor speed. The concentration distribution near the bottom of the cell is therefore closely related to the location of the wall of the cell at the cell bottom. Even more noticeable is the effect of an incorrect bottom of the cell position for floating samples, where the concentration distribution of the initial boundaries is dependent on the bottom of the cell location. For heterogeneous solutions, no single speed is optimal for all the species present. When measuring very heterogeneous systems it is beneficial to employ a multi-speed profile to extract hydrodynamic parameters for each component of the heterogeneous mixture at a speed where both sedimentation and diffusion signals can be optimally observed (Williams et al. 2018; Gorbet et al. 2018). One effect of multi-speed profiles is that at each speed the Lamm equation needs to be solved with different boundary conditions, since both meniscus and bottom of the cell position migrate outward as the rotor is stretching. To address these issues, and taking advantage of the 10 μm resolution available in the Optima AUC, we have developed a new calibration disk, experimental procedures and UltraScan (Demeler and Gorbet 2016) modules to carefully measure these effects and correct them during fitting by calibration of chromatic aberration and rotor stretch.

Materials and methods

All experiments were performed using Beckman Coulter Optima AUC™ instruments at the Canadian Center for Hydrodynamics (CCH) at the University of Lethbridge, Alberta. The Optima AUC instruments are equipped with Rayleigh interference optics, and a UV–visible absorbance spectrophotometer.

Calibration disk design

The calibration disk has a geometry with two sector-shaped channels, each divided into seven open sectors for each channel, and six ribs (see Fig. 1). Each sector is 3.7° wide, wider than a standard 2-channel epon-charcoal centerpiece, which is only 2.5° wide, and is offset by 0.9° from the centerline. A guide notch (1.6 mm \times 0.5 mm) is included to assure proper alignment within the cell housing. The innermost edge is located at 57 mm, and the outermost edge is at 71.5 mm, from the center of rotation. The center of the disk is

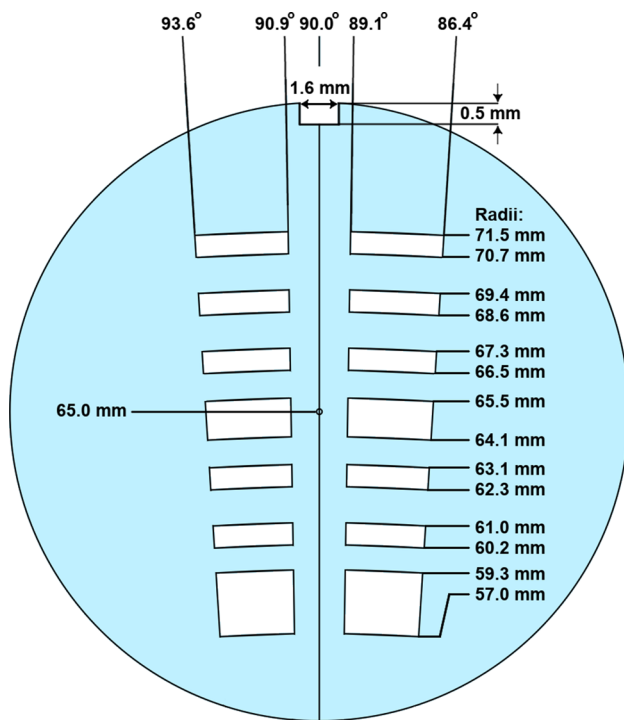


Fig. 1 Calibration disk design

located at 65 mm. Additional edges are located at 59.3 mm, 60.2 mm, 61 mm, 62.3 mm, 63.1 mm, 64.1 mm, 65.5 mm, 66.5 mm, 67.3 mm, 68.9 mm, 69.4 mm, and 70.7 mm. All edges follow a circular shape with the radius of the edge's position. In selecting this design, we considered the following requirements:

1. We maximized the number of edges to allow the acquisition of a large number of position replicates to improve the statistics of a rotor stretch protocol. For reasons related to the rotor stretch calculation algorithm, the openings were designed to be at least 500 μm to prevent overlaps in inner and outer edge position recordings when performing rotor stretch calculations. In such cases the maximum stretch will be slightly less than the distance between adjacent edges, which we never observed to exceed 400 μm , even for 25-year-old rotors spinning at 60,000 rpm. Ribs are at least 100 μm wide to assure sufficient stability when the rotor is spinning at high speed.
2. The Optima AUC uses a photomultiplier detector to detect light passing through the sample. Depending on the opaqueness of the sample, the instrument will adjust the photomultiplier voltage. The UV detector performs this check at 65.0 mm in the center of the reference channel by measuring the intensity of light passing through to the detector at this point. It is important to assure that the light path is never blocked in this position. If it were

blocked, the photomultiplier voltage would be set to the maximum gain and flood the detector with too much light in the open sections. Therefore, the 4th open section (center hole) is positioned to assure an opening for the light intensity calibration, regardless of rotor stretch. Thus, we can assure that an appropriate photomultiplier voltage can always be set, irrespective of wavelength or rotor stretch, and prevent the light path from being blocked by a solid rib.

3. At each rotor speed, a delay-time calibration procedure is performed to determine the precise angle of the rotor and to find the sample cell channels. The instrument is programmed to find the counterbalance's inner calibration holes and uses them to obtain a precise angle for the calibration hole. To replicate this feature, the innermost open sector is longer and positioned in the same position as the calibration holes of the counterbalance. This permits the calibration disk to be used for delay calibration purposes.
4. The shape of the edges follow the circle of their radii, and the sectors are wider than standard centerpieces. This minimizes any errors from lamp flash timing and improves radial recording accuracy, since, regardless of lamp flash timing variation, the same radial edge position will be recorded for each edge.
5. Both sectors are mirror images of each other. Scanning in intensity mode will allow each sector to be scanned to a separate image, and calibration results from both sectors can be compared for agreement. Any disagreement between the two sector's edge positions indicates an alignment issue with the calibration disk and can be used as a guide to correct the alignment notch of the cell housing or rotor.
6. The edge positions from our design have been verified by scanning the calibration disk on a high-resolution flatbed scanner. During the rotor stretch calibration, the analysis module in UltraScan will calculate the edge positions at rest so they can be compared to the designed positions to validate the instrument's radial calibration. The importance of the radial calibration accuracy was previously investigated by LeBrun et al. (2018), who proposed an alternative design for radial calibration verification. Focusing on radial calibration, they designed a window with precisely positioned etchings. The pattern used in the LeBrun design has a different layout in each channel and can be used for the calibration of interference optics. Since windows do not have an alignment slot for the guide rail, alignment can be an issue. In contrast to the LeBrun design, by use of correct spacer rings, our calibration disk can be positioned precisely in the focus position of the light path for optimal imaging accuracy of the edge positions.

- The calibration disk is installed between two windows and positioned in the focal point plane (2/3 of the optical plane of the 1.2 cm AUC cell housing) using appropriate spacers.

Calibration disk manufacturing

Laser cutting, 3D printing, and computer numerical control (CNC) machining were all tested for the manufacturing of the calibration disk. 3D printing has previously been used for the manufacturing of centerpieces (Desai et al. 2016), but was found to be too imprecise for our needs, and the plastics used lacked sufficient rigidity at 0.5 mm thickness. Thicker material produced measurable issues with shading on one side of the edge, suggesting that the incident beam was not perfectly perpendicular to the focus plane, either due to rotor precession or alignment issues with the optical system. CNC machining produced the most reproducible and accurate results. A Sherline 3 axis Bench Top CNC Mill with a tolerance of ± 0.005 cm, featuring a solid carbide slotting end mill, was used. Calibration disks were cut from 0.5 mm brass shim stock and were manufactured by Technical Services of the University of Lethbridge. Predicted positions were verified by scanning the calibration disk using a flatbed scanner with 3200 DPI optical resolution (~ 8 μm), by determining the actual edge positions using standard Euclidean geometry, while assuming the center of the disk to be located at 65 mm. Using this approach, each calibration disk's edge positions were individually measured and verified for their actual positions, so they could be compared with the absolute positions measured in the Optima AUC.

Rotor stretch data collection

We describe a method to measure the titanium rotor stretch for the two rotors used in AUC instruments (An60Ti, 4-hole, and An50Ti, 8-hole) as a function of speed to predict the precise movement of the radial reference frame during rotor acceleration. The following protocol is used to collect stretching data: the Optima AUC is radially calibrated with the manufacturer's counterbalance in hole 4 or 8, depending on rotor type, using the manufacturer's programmed method which calibrates at 3,000 rpm and 250 nm. This procedure can also be used for the older Proteomelab instrument, a set of files describing the experimental profile is provided in the supplementary information (rotorstretch.zip). Next, the calibration disk is sandwiched between two windows and window holders in a standard Beckman housing, which is fitted with two spacers, an 8.5 mm spacer above the upper window and a 3 mm spacer below the lower window, such that the calibration disk is positioned in the exact focal plane of the Optima AUC UV/visible detection optics (von Seggern 2020). A counterbalance or a filled cell is placed

in the opposite hole to balance the rotor. A standard epon-charcoal 2-channel centerpiece filled with 460 μl of aqueous solution in both channels will balance the calibration disk and spacer assembly when identical windows are used. The rotor is accelerated to 60,000 rpm for 10 min to assure all cell components are at equilibrium positions inside the cell housing. The rotor is then brought to rest and is temperature-equilibrated at the desired run temperature for at least 2 h under vacuum to assure any stretch hysteresis is brought back to equilibrium at rest. Calibration data is collected with a run profile that accelerates the rotor to 3000 rpm, and after a 15-min delay, scans the calibration disk at least five times. Next, the rotor is accelerated by 1000 rpm to 4000 rpm, and a second round of data collection is performed (at least five scans) after a 15-min delay. The protocol is repeated, incrementing the speed by 1000 rpm for each step, until the maximum rotor speed has been reached. The experimental data record a series of step functions for each edge position, which progressively moves to longer radii as the speed is increased (see Fig. 2). Measurements below 10,000 rpm tend to produce displacements of less than 10 μm , the stepping motor's physical resolution for the radial domain, and therefore should not be included. Rotor wobble due to slight imbalance at lower speeds could further add to uncertainty, and the data for speeds $< 10,000$ rpm should be manually inspected for stability before inclusion in a fit.

Rotor stretch analysis

We developed a utility in UltraScan to measure the rotor stretch from the calibration disk data produced from the rotor stretch calibration run profile (see “Rotor Stretch Data Collection”, Fig. 2). A step-by-step tutorial for the procedure for analyzing rotor stretch data is included in the supplementary information. A graphical routine captures any data points in the vertical edge region and averages any points originating from the same edge at each speed to obtain a single position for the edge. Multiple scans taken at each speed produce additional measurements that are averaged to obtain a better signal-to-noise ratio. Next, the radial differences between successive speeds are calculated for each edge and averaged for each speed over all edges, and plotted against rotor speed. These averages are then plotted and fitted to a second-order polynomial, which describes the stretch as a function of rotor speed (see Fig. 3):

$$r = r_0 + s_1 \text{rpm} + s_2 \text{rpm}^2 \quad (1)$$

where r_0 is the rotor stretch at rest, and s_i is the i -th stretch coefficient. A quadratic polynomial function is well suited for this fit, because the centrifugal forces increase with the square of the rotor speed. A constraint is applied that ensures that r_0 is close to zero at zero rotor speed, which allows

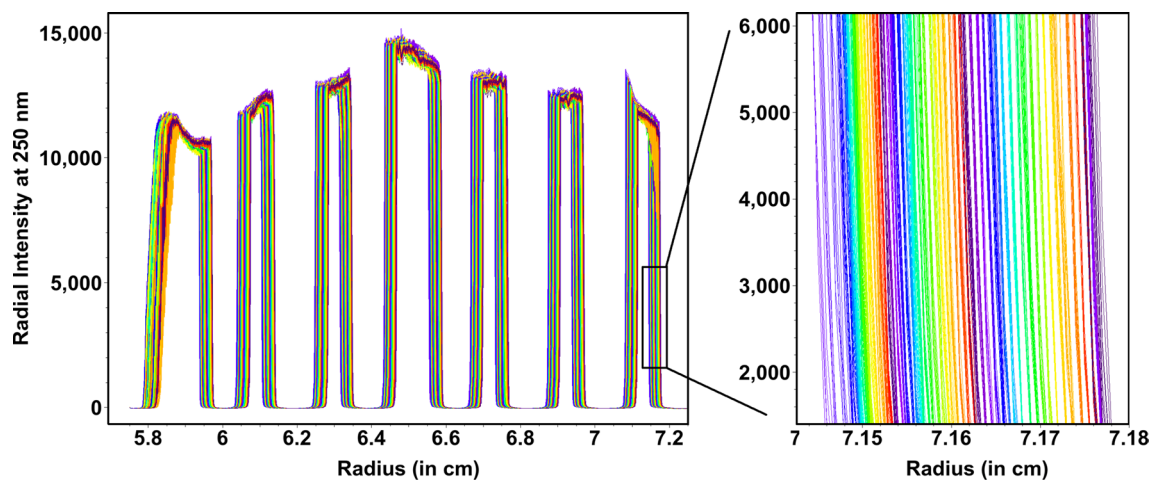


Fig. 2 Intensity rotor stretch data collected from the calibration disk for an An60Ti rotor, 0–60,000 rpm in 1000 rpm steps. Insert: Zoomed region shows the quadratic change in stretch spacing depend-

ence on rotor speed. Color changes from blue, green, yellow to red as the speed increases

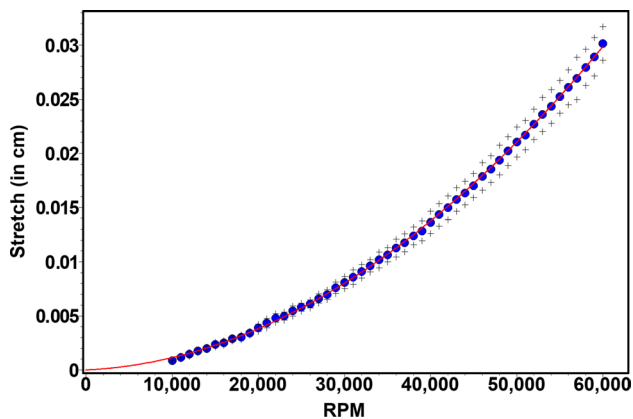


Fig. 3 Blue: Rotor stretching data for An60Ti rotor between 10,000–60,000 rpm. Red: second order polynomial fit. Black crosses: standard deviation

absolute displacements to be obtained from the fit. The fitting profiles are saved in the LIMS database (Brookes et al. 2013), where stretch profiles for different temperatures and centerpiece types (e.g., epon vs. titanium) can be stored for each rotor. At this point, a prediction can be made about the absolute position of a cell bottom for each rotor speed by adding the calculated displacement to the measured cell bottom from each cell type. In UltraScan, each commonly used cell type is scanned and measured for the absolute position of the bottom of the cell. All major centerpiece types commercially available have been measured by us and programmed in the UltraScan LIMS database for all users. Using the rotor stretch calculation together with the measured cell bottom for a particular cell, appropriate corrections are made automatically in UltraScan to the boundary

conditions for any experimental data set, ensuring optimal estimates for the boundary conditions, and appropriate solutions for the Lamm equation. Cell dimensions and geometries and rotor stretch calibrations are stored in the LIMS database and queried in real-time during analysis to provide optimal boundary conditions. Rotor stretch measurements performed with a previous generation of calibration disk that employed rectangular sectors instead of sectors with edges that follow the radial arc produced significantly noisier data and are no longer recommended for use in rotor calibrations (Gorbet et al. 2018).

Chromatic aberration correction

The Optima AUC offers the ability to collect data for up to one hundred user-selectable wavelengths between 190–800 nm during a single experiment. Scanning the calibration disk at different wavelengths revealed that chromatic aberration effects cause different radial positions to be recorded for the same physical location in the AUC cell. Based on measurements from seven Optima AUC instruments, we recorded total radial deviations for different instruments ranging between 40–380 μm across the entire wavelength range. An error of 380 μm in the radial measurement contributes as much as 0.66% error to the measurement of a sedimentation coefficient, with the largest errors observed near the top of the cell, and decreasing towards the bottom as the total percentage of radial error decreases as well. This means that not only the absolute measurement is incorrect, but the radial deviation also contributes to an apparently non-constant s value (Eq. 2 can be used to calculate sedimentation coefficient errors).

$$s_b = \ln\left(\frac{r_b}{r_m}\right) (\omega^2(\Delta t))^{-1} \tag{2}$$

where s_b is the apparent sedimentation coefficient of a particle having sedimented from meniscus position r_m to boundary position r_b with angular velocity ω during elapsed time Δt .

We believe the deviations result from imperfections in the Optima’s optical system, most likely from non-vertical light beam tracing, though the exact cause has not been identified at the time of this writing. A careful review of factors that need to be considered in the design of mirror-based optical systems for AUC instruments can be found in reference (Pearson et al. 2018). The lack of perpendicular incident light is also supported by the appearance of shadows on one side of the calibration disk edges, producing a zig-zag effect in the deviations from the predicted positions (Fig. 4). On one of our instruments the shadow effect appeared to be most pronounced at very long and very short wavelengths. Furthermore, we observed a wavelength-dependent variability in the radial scaling between the top and the bottom of the cell. A change in the absolute deviation was observed when inner edge deviations were compared with outer edge deviations. For longer wavelengths, the measured edge positions deviated from the known positions by a larger amount at long radii than at positions closer to the rotor center. At short wavelengths (200 nm) the offsets deviated by the same amount at the top and the bottom of the cell. The magnitude of the total offset was most pronounced for shorter wavelength (Fig. 4), and depended on the instrument used for the calibration. This result is summarized in Fig. 5, which shows the deviations as a function of the slopes and intercepts of the linear fits in Fig. 4. On a second Optima AUC instrument

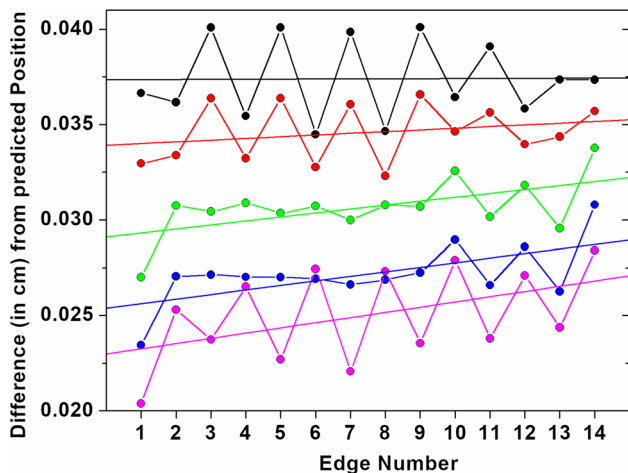


Fig. 4 Edge position deviations from predicted positions for observations made at 200 nm (black), 230 nm (red), 300 nm (green), 460 nm (blue), 750 nm (magenta)

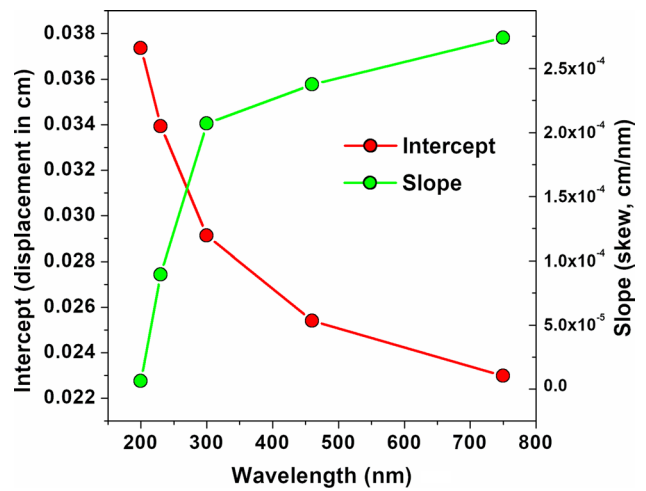


Fig. 5 Wavelength-dependent deviations of radial positions recorded in the Optima AUC. Absolute offsets of the inner edge (intercepts from linear fits in Fig. 4, red) and deviations across the calibration disk (fitted slopes from Fig. 4, green)

in our lab, a similar observation is made, however, the absolute deviation of the measured edge position compared to the predicted edge position is smaller. Deviations of measured and predicted radial edge positions are listed in Table 1.

To correct for chromatic aberration, a calibration curve based on the shift in edge position as a function of wavelength is constructed to correct the wavelength-dependent variations observed in any instrument. As an alternative, the meniscus positions of 4–8 sample channels filled with 0.23 ml of water can be repeatedly scanned in intensity mode at 62 wavelengths, spanning 190–800 nm in 10 nm increments. A speed of 14,000 rpm is recommended to minimize the time required for each scan, since at 14,000 rpm the

Table 1 Edge positions in cm at rest, measured at 250 nm (same as radial calibration wavelength) vs. predicted

Edge	Measured	Predicted	Difference
1	5.94974	5.929	– 2.07E-02
2	6.05122	6.025	– 2.62E-02
3	6.11951	6.097	– 2.25E-02
4	6.26084	6.237	– 2.38E-02
5	6.32905	6.308	– 2.11E-02
6	6.44025	6.425	– 1.53E-02
7	6.56951	6.55	– 1.95E-02
8	6.67923	6.658	– 2.12E-02
9	6.74475	6.728	– 1.68E-02
10	6.88611	6.868	– 1.81E-02
11	6.95078	6.939	– 1.18E-02
12	7.09261	7.077	– 1.56E-02
13	7.15398	7.146	– 7.98E-03

rotor speed is optimally synchronized with the flash rate of the flash lamp. To build a calibration file from the meniscus position scans collected as described above, the following procedure is recommended: First, the calibration data are imported into UltraScan from the “View Raw Optima Data” menu entry in the “Utilities” menu. Once the data are downloaded and displayed in the data viewer, the user zooms the meniscus region (still in intensity mode) for each channel. For each channel, a csv formatted spreadsheet is generated in the UltraScan imports data folder for the dataset that maps the radial position of the meniscus minimum against the wavelength. Using a third party spreadsheet program like Excel or Origin, the csv files are averaged, and the 250 nm value is subtracted from each wavelength’s radial position. The 250 nm position presumably is correct because the instrument was radially calibrated with the manufacturer’s counterbalance at 250 nm, and will be used as the true offset with zero correction. A parameterizing curve is fitted (with 1 nm increments) to the average curve which follows the chromatic aberration profile as shown in Fig. 6, and uploaded in the “Edit: Preferences: Instrument Preferences” instrument configuration.

A routine is implemented in UltraScan to extract the wavelength dependent variations either from the calibration disk or the meniscus positions. Data from multiple channels should be averaged to improve the signal-to-noise ratio. The resulting data can be fitted to an appropriate parameterization function using standard data fitting software. This function, and the shape of the observed aberration curve, varied significantly for each instrument we tested, including the maximum deviation observed. An example is shown

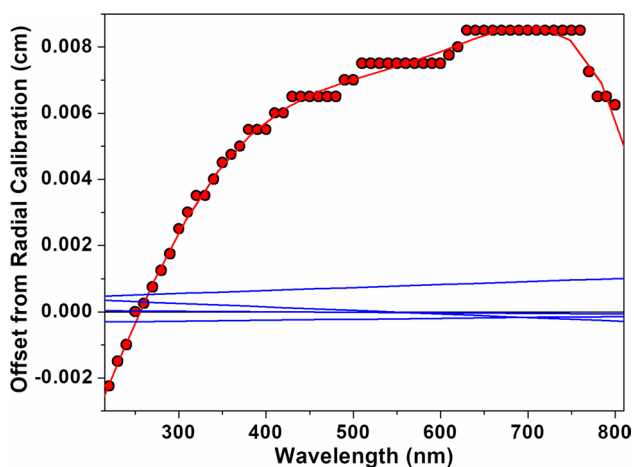


Fig. 6 Example of chromatic aberration error in the Optima AUC. Red: DEVIATION from radial calibration at 250 nm from four averaged meniscus positions, fitted to a 5th-order polynomial. Blue: Observed meniscus positions of the four input menisci after correction, all four showing <0.001 cm error. Note: The data reported here was recorded on a different instrument than the data shown in Figs. 4, 5

in Fig. 6. The parameterization function is used to generate a radial correction array for all wavelengths between 190–800 nm. This array is uploaded to the UltraScan LIMS database. Before constructing a correction array, a radial calibration is performed at 250 nm using the manufacturer provided experimental protocol. The 250 nm radial position is assumed to provide the true radial position. Deviations from this value determined for all other wavelengths are subtracted from each radial position of the experimental data during import into the UltraScan LIMS database. The corrected data deviates less than 10 μm across the entire wavelength spectrum from the radial positions observed at the calibration wavelength (Fig. 6, blue lines).

Rotor stretch calibration results

A calibration disk was designed to measure highly accurate and reproducible rotor stretching profiles for Beckman’s An50Ti and An60Ti analytical titanium rotors. Calibration modules developed for UltraScan derive rotor stretch profiles from 13 arc-shaped edges, generating fits with much improved fitting statistics over previous generations of calibration disks. Rotor stretch calibrations resulted in highly reproducible rotor stretch fits that varied by less than 0.25% in the maximum stretch (at 60,000 rpm) predicted between experiments for the same rotor at 20 °C, and a maximum of 0.88% when rotor stretch was compared for the same rotor across three different temperatures (4 °C, 20 °C and 37 °C). This finding is consistent with previous research on the physical properties for titanium (Chu and Steeves 2011; Steeves et al. 2009), suggesting minimal change in radial position as a function of temperature change. However, maximum stretch values at 60,000 rpm from 3 different rotors of the same type (AN60Ti) varied by as much as 3% when measured at the same temperature. Predicted values for 50,000 rpm showed that An50Ti rotors stretched more than An60Ti rotors by an average of 4.3%. The amount of maximum stretch determined for different rotors did not correlate with the age of the rotor. The calibration results for measurements from five different rotors in use in our facility are summarized in Table 2.

We also investigated the hysteresis of rotor stretch. It appeared that stretching and contracting in response to acceleration and deceleration are immediate and reversible. In fact, changes in stretch manifest themselves in measurable adiabatic temperature changes in the rotor, causing adiabatic cooling of the rotor during acceleration, and adiabatic heating during deceleration (see Fig. 7). As can be seen in this figure, the magnitude of this exothermic and endothermic adiabatic effect is approximately equal, considering that the temperature is also affected by the thermostat response of the instrument in response to rotor temperature change.

Table 2 Rotor stretch calibration results in cm for five rotors in use at the Canadian Center for Hydrodynamics

Rotor	Type	Temperature (°C)	50 krpm stretch	60 krpm stretch
17u900	AN50	20	0.02228	0.03163
97u378	AN50	20	0.02252	0.03176
00u569	AN60	20	0.02124	0.02982
18u919	AN60	20	0.02184	0.03038
92u341-a	AN60	20	0.02137	0.03022
92u341-b	AN60	20	0.02145	0.03030
92u341	AN60	4	0.02152	0.03043
92u341	AN60	37	0.02141	0.03049

Stretch values are theoretical values predicted from individual fits for each rotor to Eq. 1

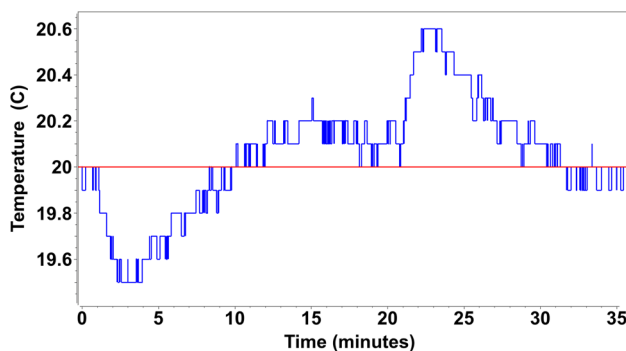


Fig. 7 Example of adiabatic temperature change of the rotor during rotor acceleration to 60,000 rpm (endothermic, 0–2.5 min), temperature equilibration at 60 krpm (2.5–21 min), deceleration to 0 rpm (exothermic, 21–23 min), and temperature equilibration to baseline 20°C (21–35 min) measured in the Optima AUC

Discussion

The development of a new calibration disk for the analytical ultracentrifuge supports accurate and highly reproducible calibration of rotor stretch profiles for AN50Ti and AN60Ti rotors. Our choice of material offers mechanical rigidity even at high rotor speeds. An arc-shaped edge contributes to improved noise characteristics. The prediction of rotor stretch imposed translocation of the reference frame as a function of speed can be made well within the mechanical resolution of the Optima AUC's stepping motor (10 μm), and can be used to accurately predict the bottom boundary condition of a cell at any speed. Importantly, together with accurately measured centerpiece geometry, this information obviates the need for fitting the cell bottom position, allowing more accurate fits with Lamm equation models by providing more accurate boundary conditions for their solution. This is particularly important for samples that float or sediment slowly with a

large back-diffusion signal which is sensitive to the bottom position of the cell. Furthermore, the calibration disk can be used to confirm the radial calibration of the instrument by comparing independently measured edge positions with measured values in the instrument. We are currently unable to identify the source of the relatively large deviations (80–260 μm , Table 1) between radial edge positions predicted by our scanned measurements from the positions observed in the flatbed scanner, as well as the radial dependence of these deviations. A possible error source is rotor precession or imprecise radial calibration, since this observation changes between instruments. Other possibilities include manufacturing variations between rotor hole centers, and the possibility for the calibration centerpiece not being perfectly centered in the cell housing. All of our measurements were preceded by a radial calibration procedure as recommended by the manufacturer with a newer counterbalance (less than 2 years old). Further investigations will be necessary to identify the source of these deviations. Our data showed that temperature had little effect on the stretch profiles of titanium rotors, they varied by less than 3 μm for temperatures ranging between 4–37 $^{\circ}\text{C}$, which is outside of the radial resolution of the Optima AUC. We therefore conclude that temperature effects on the stretch profile of the titanium rotors used in the Optima AUC can be ignored within the operating temperature range of the instrument. Variations between individual rotors and 4-hole and 8-hole rotors are larger and we recommend separate calibration profiles for optimal accuracy. The calibration disk design also supports delay calibration, and in combination with appropriate spacers to position the calibration disk in the focus plane, the weight of an assembled housing with the calibration disk can be matched with a filled epon-2-channel centerpiece assembly by using two sapphire windows in the sample cell, and one sapphire and one quartz window in the calibration disk cell, so it can be used in hole 4 or 8 as a reference standard for AUC experiments performed under Good Manufacturing Protocols (GMP).

The calibration disk can further be used to estimate the radial error resulting from chromatic aberration. These artifacts cause a wavelength-dependent radial error between 40–380 μm , varying between instruments, but are corrected by programmable software adjustments in UltraScan that utilize the calibration disk for a chromatic correction profile that is stored in the LIMS database and automatically applied during import of experimental data. These corrections reduce chromatic aberration errors to less than 10 μm , the physical resolution of the Optima AUC, and significantly improve fitting accuracy for multi-wavelength experiments. We have shown that our calibration disk design for the Optima AUC can provide valuable improvements and accuracy enhancements for modeling of sedimentation velocity

experiments, and results in improved boundary condition estimates for Lamm equation solutions. The calibration disk's design allows it to be used in place of a counterbalance in routine experiments as an additional reference material for GMP experiments. Importantly, we have shown that the Optima AUC's radial recording capability is reproducible beyond its physical resolution of 10 μm , and systematic errors resulting from instrument-specific chromatic aberrations can be effectively corrected in software until a more permanent hardware correction is made.

Acknowledgements This work was supported by the Canadian Foundation for Innovation, the Canada 150 Research Chairs program, the Canada Foundation for Innovation Grant CFI-37589, National Institutes of Health grant 1R01GM120600, NSERC DG-RGPIN-2019-05637, a CIHR foundation grant (FDN 148469), and the Chinook Summer Studentship Award. Special thanks to Denton Fredrickson.

References

- Brookes EH, Demeler B (2006) Genetic Algorithm Optimization for obtaining accurate molecular weight distributions from sedimentation velocity experiments. In: Wandrey C, Cölfen H (eds) Analytical ultracentrifugation VIII, progress in colloid polymer science. Springer, New York
- Brookes EH, Demeler B (2007) Parsimonious regularization using genetic algorithms applied to the analysis of analytical ultracentrifugation experiments. In: GECCO Proceedings ACM
- Brookes E, Demeler B (2008) Parallel computational techniques for the analysis of sedimentation velocity experiments in UltraScan. *Colloid Polym Sci* 286(2):138–148
- Brookes EH, Cao W, Demeler B (2010) A two-dimensional spectrum analysis for sedimentation velocity experiments of mixtures with heterogeneity in molecular weight and shape. *Eur Biophys J* 39:405–414
- Brookes E, Singh R, Pierce M, Marru S, Demeler B, Rocco M (2013) US-SOMO cluster methods: year one perspective. In: XSEDE '13 Proceedings of the Conference on Extreme Science and Engineering discovery Environment: Gateway to discovery Article No. 65 ACM New York, NY, USA 2013 ISBN: 978-1-4503-2170-9
- Cao W, Demeler B (2005) Modeling analytical ultracentrifugation experiments with an adaptive space-time finite element solution of the Lamm equation. *Biophys J* 89(3):1589–1602
- Cao W, Demeler B (2008) Modeling analytical ultracentrifugation experiments with an adaptive space-time finite element solution for multi-component reacting systems. *Biophys J* 95(1):54–65
- Carruthers LM, Schirf VR, Demeler B, Hansen JC (2000) Sedimentation velocity analysis of macromolecular assemblies. *Method Enzymol Numer Comput Methods* 321:66–80
- Chu JJ, Steeves CA (2011) Thermal expansion and recrystallization of amorphous Al and Ti: a molecular dynamics study. *J Non-Cryst Solids* 357(22–23):3765–3773
- Demeler B (2010) Methods for the design and analysis of sedimentation velocity and sedimentation equilibrium experiments with proteins. *Cur Protoc Prot Sci* 7:7–13
- Demeler B (2019) Measuring molecular interactions in solution using multi-wavelength analytical ultracentrifugation: combining spectral analysis with hydrodynamics Biophysics using physics to explore biological systems. *Biochemist* 41(2):14–18
- Demeler B, Brookes EH (2008) Monte Carlo analysis of sedimentation experiments. *Colloid Polym Sci* 286:129–137
- Demeler B, Gorbet G (2016) Analytical ultracentrifugation data analysis with UltraScan-III. In: Uchiyama S, Stafford WF, Laue T (eds) Analytical ultracentrifugation: instrumentation, software, and applications. Springer, Berlin
- Demeler B, Brookes E, Wang R, Schirf V, Kim CA (2010) Characterization of reversible associations by sedimentation velocity with ultrascan. *Macromol Biosci Macromol Biosci* 10(7):775–782
- Desai A, Krynitsky J, Pohida TJ, Zhao H, Schuck P (2016) 3D-Printing for analytical ultracentrifugation. *PLoS ONE* 11(8):e0155201
- Gorbet GE, Pearson JZ, Demeler AK, Cölfen H, Demeler B (2015) Next-generation AUC: analysis of multiwavelength analytical ultracentrifugation data. *Methods Enzymol* 562:27–47. <https://doi.org/10.1016/bs.mie.2015.04.013>
- Gorbet GE, Mohapatra S, Demeler B (2018) Multi-speed sedimentation velocity implementation in UltraScan-III. *Eur Biophys J* 47(7):825–835. <https://doi.org/10.1007/s00249-018-1297-z>
- Hu J, Soraiz EH, Johnson CN, Demeler B, Brancalion L (2019) Novel combinations of experimental and computational analysis tested on the binding of metalloprotoporphyrins to albumin. *Int J Biol Macromol* 1(134):445–457
- Johnson CN, Gorbet GE, Ramsower H, Urquidi J, Brancalion L, Demeler B (2018) Multi-wavelength analytical ultracentrifugation of human serum albumin complexed with porphyrin. *Eur Biophys J* 115(2):328–340
- Lamm O (1929) Die Differentialgleichung der Ultrazentrifugierung. *Ark Mat Astron Fys* 21B:1–4
- LeBrun T, Schuck P, Wei R, Yoon JS, Dong X, Morgan NY, Fagan J, Zhao H (2018) A radial calibration window for analytical ultracentrifugation. *PLoS ONE* 13(7):e0201529
- Liu J, Shire SJ (1999) Analytical ultracentrifugation in the pharmaceutical industry. *J Pharm Sci* 88(12):1237–1241
- Patel TR, Winzor DJ, Scott DJ (2016) Analytical ultracentrifugation: a versatile tool for the characterisation of macromolecular complexes in solution. *Methods* 95:55–61
- Pearson J, Hofstetter M, Dekorsy T, Totzeck M, Cölfen H (2018) Design concepts in absorbance optical systems for analytical ultracentrifugation. *Analyst* 143(17):4040–4050
- Plascencia-Villa G, Demeler B, Whetten RL, Griffith WP, Alvarez M, Black DM, José-Yacamán M (2016) Analytical characterization of size-dependent properties of larger aqueous gold nanoclusters. *J Phys Chem C* 120(16):8950–8958
- Steeves CA, Mercer C, Antinucci E, He MY, Evans AG (2009) Experimental investigation of the thermal properties of low expansion lattices. *Int J Mech Mater Des* 5(2):195–202
- Svedberg T, Pedersen K (1940) The ultracentrifuge. Oxford University Press, London
- von Seggern E (2020) Personal communication. Beckman Coulter R and D, Loveland, Colorado
- Williams TL, Gorbet GE, Demeler B (2018) Multi-speed sedimentation velocity simulations with UltraScan-III. *Eur Biophys J* 47(7):815–823. <https://doi.org/10.1007/s00249-018-1308-0>
- Zhang J, Pearson JZ, Gorbet GE, Cölfen H, Germann MW, Brinton MA, Demeler B (2017) Spectral and hydrodynamic analysis of west Nile virus RNA-protein interactions by multiwavelength sedimentation velocity in the analytical ultracentrifuge. *Anal Chem* 89(1):862–870 PMID: 27977168
- Zhao H, Ghirlando R, Alfonso C et al (2015) A multilaboratory comparison of calibration accuracy and the performance of external references in analytical ultracentrifugation. *PLoS ONE* 10(5):e0126420

Publisher's Note Springer Nature remains neutral with regard to jurisdictional claims in published maps and institutional affiliations.